

## V. Methods of Empirical Analysis

### V.1 Basic Objectives

After obtaining experimental data such as those discussed in the previous chapter, it is necessary to extract from the data numerical values of transport coefficients such as  $D_{xx}$  and  $D_{LL}$ , in order best to describe the observations in the context of magnetospheric diffusion processes. This must be done with the realization that such a course of action (and the parameters determined from it) are subject to uncertainties, including the question as to whether the observations can actually be described in terms of the diffusion processes selected.

At present, the most desirable course to take in verifying the validity of the diffusion equation adopted for describing a given set of magnetospheric particle observations is to use a self-consistent analysis. In a self-consistent approach, the values of the transport coefficients should be determined (as far as possible) empirically from the particle data. After values for the coefficients are so estimated, the model should be verified by inserting these values in the appropriate diffusion equation to show that the model indeed predicts the observed spatial structure and/or temporal evolution of the particle data. Subsequently, the magnitudes of the transport coefficients should be manipulated (by the methods of Chapters II and III) to yield predictions for the spectral densities of magnetospheric field fluctuations (waves, impulses, *etc.*). Finally, these predictions should be compared with available observations of magnetospheric field and wave activity (see Section IV.7).

An empirical determination of the transport coefficients directly from the measured particle data presents certain difficulties. Frequently, such a determination is arrived at by making initial assumptions concerning the relative importance of the various diffusion mechanisms. Often the transport coefficient associated with the dominant process can be determined only by assigning to the other (secondary) process a fixed and somewhat arbitrary value. Moreover, it is usually necessary to assume that the transport coefficients are time-independent, or else related in some fixed way to the geomagnetic indices ( $K_p$ ,  $D_{SI}$ , *etc.*).

For example, a common procedure not readily justified is that of directly relating the *apparent* electron-flux decay rates to numerical values of the pitch-angle diffusion coefficient  $D_{xx}$ . This approach, in

which it is assumed (*cf.* Section II.7) that  $D_{xx} \sim -(x_c^2/5)(\partial \ln \bar{f} / \partial t)_{E, x_s}$  is based on the expectation that the electron pitch-angle distribution is in its lowest eigenmode. The "decay" times shown in Fig. 41 (Section IV.3) have been obtained under this assumption.

A difficulty in this approach is illustrated by the  $L=4$  electron data ( $E > 1.0$  MeV) plotted in Fig. 38. During the first several days following each of the four largest magnetic storms, the electron flux did not appear to decay at all, but rather remained constant or increased in intensity. Thus, it would not have been possible to read a pitch-angle diffusion coefficient directly from these data. Electron losses undoubtedly occurred during these periods, but the temporal flux changes were probably dominated by radial-diffusion effects (*cf.* Figs. 52 and 53, Section IV.6).

Additional opportunities for determining the pitch-angle diffusion coefficient are provided by the data showing the azimuthal variation of precipitating electron fluxes (Fig. 36, Section IV.2) and the data showing relaxation of electron pitch-angle distributions to their lowest eigenmode (Fig. 34, Section IV.2). In these cases it is impossible to read  $D_{xx}$  directly from the data, and so more sophisticated analytical techniques are required (see Section V.2). Application of such techniques may yield both a nominal value and functional form for  $D_{xx}$ .

In the case of radial diffusion, several techniques and procedures have been developed for extracting  $D_{LL}$  from the observations. The choice of method depends in part on whether the data provide stationary (*cf.* Section IV.5) or time-varying (Section IV.6) flux profiles. As noted in Section IV.6, it is very helpful to have data in several energy channels in order to characterize the actual particle spectrum. Such spectral information affords considerable freedom in the choice of method for extracting  $D_{LL}$ .

When the data consist solely of "stationary" flux profiles, it is generally necessary to assign either  $D_{xx}$  or  $D_{LL}$  somewhat arbitrarily in order to extract the other. In the event that the data are obtained from the region of the magnetosphere where atmospheric losses predominate over wave-particle scattering, it is appropriate to insert  $D_{xx}$  as a known function of  $M$ ,  $J$ , and  $\Phi$  [*cf.* (2.17), Section II.2]. Outside the region where atmospheric scattering losses predominate, it is usually necessary to assign the observed "lifetimes" (as from Fig. 41, Section IV.3) characteristic of geomagnetically more active time periods (when the flux profiles typically are not stationary). Then, treating the relevant diffusion equation (see Sections III.7 and III.8) as a linear first-order differential equation for  $D_{LL}$ , it is possible to express the solution as a *spatial quadrature*, *i.e.*, an integral with respect to  $L$  (see Section V.3). For this purpose, the derivatives of  $\bar{f}$  are obtained numerically from the observational data. The radial-diffusion coefficient  $D_{LL}$  thus extracted

from the data can subsequently be verified by obtaining the steady-state solution of the diffusion equation, *i. e.*, by *spatially integrating* the equation (see Section V.7) for  $\bar{f}(M, J, \Phi)$ . If this solution reproduces the observed steady-state profiles, then the value obtained for  $D_{LL}$  is considered reliable. If not, then either  $D_{LL}$  must be adjusted to yield a better fit, or the underlying model of the competing processes (*e. g.*, the arbitrarily assigned value of  $D_{xx}$ ) must be modified.

Additional opportunities for empirical analysis arise if the observed flux profiles vary with time. The temporal coordinate adds a new dimension to the problem and makes it possible (in principle) to extract both  $D_{LL}$  and  $D_{xx}$  (as functions of  $L$ ) from the data simultaneously. The introduction of a *variational technique* (see Section V.5) serves this purpose well. Simpler techniques allow either  $D_{xx}$  or  $D_{LL}$  to be expressed in terms of *quadratures* (Section V.4) over the data if the other diffusion coefficient is specified *a priori*. The ultimate test of the numerical validity of  $D_{xx}$  and  $D_{LL}$  obtained by any method is provided by a comparison of the data with the time-dependent solution of the diffusion equation, as obtained by *temporal integration* (Section V.6). In the present chapter, these various analytical methods for extracting diffusion coefficients from the data are discussed in a somewhat logical sequence.

## V.2 Pitch-Angle Eigenmodes

Pitch-angle diffusion at constant energy is governed by (2.73), an equation that can also be written in the form

$$\frac{\partial \bar{f}}{\partial t} = \frac{1}{x} \frac{\partial}{\partial x} \left[ x D_{xx} \frac{\partial \bar{f}}{\partial x} \right]_E - \frac{x}{y} D_{xx} \frac{T'(y)}{T(y)} \left[ \frac{\partial \bar{f}}{\partial x} \right]_E, \quad (5.01)$$

since  $x^2 + y^2 = 1$ . The second term of (5.01) is negligible for  $x^2 \ll 1$ . The approximation of omitting it altogether by taking  $T(y) \equiv T(1)$  converts (5.01) to a diffusion equation in cylindrical coordinates. The eigenfunctions of (5.01) for an  $x$ -independent diffusion coefficient  $D_{xx}$  would then be Bessel functions of order zero (*cf.* Section II.7). In terms of (3.51) this would mean that the typical eigenfunction  $g_n(x)$  is given by  $g_n(x) = [2/T(1)]^{1/2} [1/x_c J_1(\kappa_n)] J_0(\kappa_n x/x_c)$ , where  $J_0(\kappa_n) = 0$ . The corresponding eigenvalues  $\lambda_n$  of (3.52b) would then be of the form  $\lambda_n = (\kappa_n/x_c)^2 D_{xx}$ .

Generally, a source<sup>46</sup> term must be added to (5.01) in order to describe the evolution of  $\bar{f}$  toward a steady-state distribution. If an

<sup>46</sup>In this section, the source can be regarded either as a true source or as a simulation of the radial-diffusion term omitted from (5.01).

isotropic source term is added to (5.01) [*cf.* (3.57a), Section III.8], then the pitch-angle distribution function  $\bar{f}(x, t)$  will evolve in time toward the steady-state solution

$$\bar{f}_{\infty}(x) = (S x_c^2 / 4 D_{xx}) [1 - (x/x_c)^2] \quad (5.02)$$

for  $T(y) \equiv T(1)$  and  $D_{xx}$  independent of  $x$ . Equation (5.02) is reminiscent of (2.64) for  $s = 1$  (see Section II.6).

The 28 October 1962 nuclear blast had injected electrons with an off-equatorial maximum that subsequently decayed with time (Fig. 34, Section IV.2). The decay of the omnidirectional flux ( $E > 1.9$  MeV) can be simulated by expressing the pitch-angle distribution  $\bar{f}(x, t)$  in terms of its steady-state solution and higher-order eigenmodes, *i. e.*,

$$\bar{f}(x, t) = \bar{f}_{\infty}(x) + \bar{f}_{\infty}(0) \sum_n a_n(t) J_0(\kappa_n x/x_c) \quad (5.03)$$

with  $a_0(0) = 50/3$  and  $a_1(0) = -a_2(0) = -55/3$ . The artificial enhancement (Day 301.3) corresponds to  $t = 0$ , and  $a_n(0)$  is assumed to vanish for  $n > 2$ .

The temporal decay of  $\bar{f}(x, t)$  to  $\bar{f}_{\infty}(x)$  obtained from (5.03) by assuming  $x_c = 0.94$  and  $D_{xx} = 10^{-2} \text{ day}^{-1}$  is indicated in Fig. 68a [43]. The eigenvalues  $\lambda_n = (\kappa_n/x_c)^2 D_{xx}$  are given by  $\lambda_0 = 0.190$ ,  $\lambda_1 = 0.077$ ,  $\lambda_2 = 6.545 \times 10^{-2} \text{ day}^{-1}$ . The differential omnidirectional flux at any point on the field line is given [*cf.* (1.22), Section I.4] by

$$\begin{aligned} J_{4\pi}(X, t) &= 4\pi p^2 \int_0^1 \bar{f}(x, t) d(\cos \alpha) \\ &= 4\pi p^2 \int_x^{x_c} \left[ \frac{1 - X^2}{x^2 - X^2} \right]^{1/2} \frac{x \bar{f}(x, t)}{1 - X^2} dx, \end{aligned} \quad (5.04a)$$

where

$$X^2 \equiv 1 - (B_e/B) = (x^2 - \cos^2 \alpha) \csc^2 \alpha. \quad (5.04b)$$

The coordinate  $X$  locates a point on any field line in terms of the local field intensity  $B$  relative to the minimum (or equatorial) field intensity  $B_e$  on that field line (*cf.* Section I.4). If  $D_{xx}$  and  $x_c$  are independent of energy (as assumed above), then pitch-angle diffusion leaves the form of the energy spectrum used in (5.03) invariant. The *integral* omnidirectional flux  $I_{4\pi}(X, t)$  will then scale as  $J_{4\pi}(X, t)$ , which is plotted in Fig. 68b. The predicted evolution of  $I_{4\pi}(X, t)$  thus resembles the observed evolution (Fig. 34) rather closely.

In both the observed and predicted  $I_{4\pi}(X, t)$ , the off-equatorial ( $X > 0$ ) peak disappears as the pitch-angle distribution approaches its lowest decaying eigenmode. From  $t \sim 10$  days onward, there is very little change in the form of the pitch-angle distribution (Fig. 68a). This means only

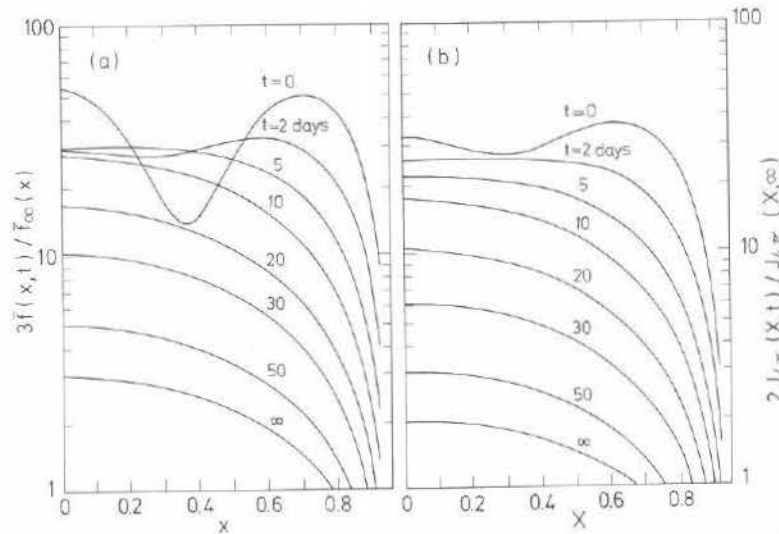


Fig. 68. Decay of equatorial pitch-angle distribution (a) and off-equatorial distribution of omnidirectional flux (b) to steady state (cf. Fig. 34), assuming  $D_{xx} = 10^{-2} \text{ day}^{-1}$  and  $x_c = 0.94$  [43].

that the lowest eigenfunction, namely  $J_0(\kappa_0 x/x_c)$ , qualitatively resembles  $1 - (x/x_c)^2$ , which contains the entire pitch-angle dependence of  $\bar{f}_\infty(x)$  for an isotropic source  $S$  [cf. (5.02)] if  $D_{xx}$  is independent of  $x$ .

The resemblance between  $g_0(x)$  and  $\bar{f}_\infty(x)$  exists even when  $D_{xx}$  varies with  $x$ . For example, if  $D_{xx}$  is proportional to  $(x/x_c)^{2\sigma}$  with  $\sigma < 1$ , it is possible to integrate the equation [cf. (5.01)]

$$\frac{1}{x} \frac{d}{dx} \left[ x D_{xx} \frac{d\bar{f}_\infty}{dx} \right] + S = 0, \quad (5.05 \text{ a})$$

with the boundary condition that  $\bar{f}_\infty(x_c) = 0$ , so as to obtain

$$\bar{f}_\infty(x) = [S x_c^2 / 4(1 - \sigma) D_{xx}] (x/x_c)^{2\sigma} [1 - (x/x_c)^{2-2\sigma}] \quad (5.05 \text{ b})$$

under the assumption that  $\partial S / \partial x = 0$ . On the other hand, the normalized eigenfunctions of (3.52b) and (3.53) for  $T(y) \equiv T(1)$  are given by

$$g_n(x) = -[2(1 - \sigma) / T(1)]^{1/2} [1/x_c J'_v(\kappa_{vn})] \times (x_c/x)^\sigma J_v(\kappa_{vn} x^{1-\sigma}/x_c^{1-\sigma}) \quad (5.06 \text{ a})$$

where  $v \equiv \sigma / (1 - \sigma)$  and  $J_\nu(\kappa_{vn}) = 0$  ( $n = 0, 1, 2, \dots$ ). The corresponding eigenvalues are given by

$$\lambda_n = (1 - \sigma)^2 (\kappa_{vn}/x_c)^2 (x_c/x)^{2\sigma} D_{xx}. \quad (5.06 \text{ b})$$

Recall that  $(x_c/x)^{2\sigma} D_{xx}$  is independent of  $x$  both in (5.06) and in (5.05). As shown in Fig. 69, where  $x_c = 0.9$ , there is a close qualitative resemblance between  $g_0(x)/g_0(0)$  and  $\bar{f}_\infty(x)/\bar{f}_\infty(0)$  for  $|\sigma| \leq 1/4$ . Thus, the form of the pitch-angle distribution changes very little between the exponential-decay phase (see Fig. 34, Section IV.2) and the steady state.

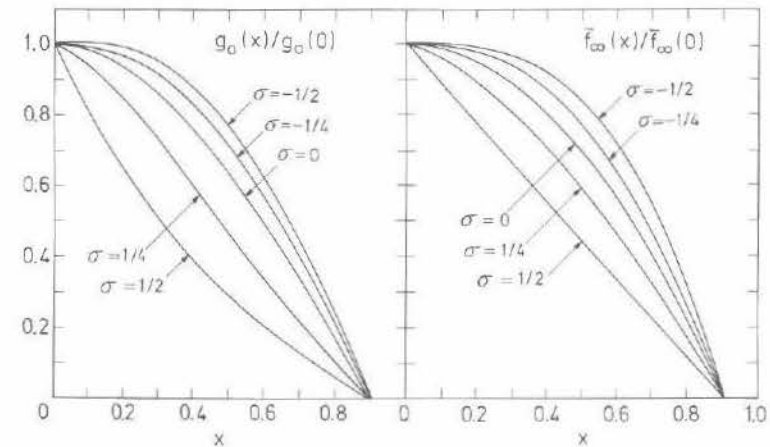


Fig. 69. Lowest eigenmode (left panel) and asymptotic steady state (right panel) for pitch-angle diffusion with  $D_{xx} \propto (x/x_c)^{2\sigma}$  and  $x_c = 0.9$ ; steady state assumes isotropic source [43].

For  $\sigma > 0$  the pitch-angle diffusion coefficient vanishes at  $x = 0$ . Consequently, the functions  $g_0(x)$  and  $\bar{f}_\infty(x)$  are more sharply peaked at  $x = 0$  for  $\sigma > 0$  than for  $\sigma = 0$ . Conversely, if  $\sigma < 0$  the pitch angle distribution tends toward a broader shape, hence a steeper gradient at  $x = x_c$ . In either case, the value of  $D_{xx}$  at  $x = x_c$  remains finite. Moreover, the values of  $(1 - \sigma)\kappa_{vn}$  that appear in (5.06b) are only moderately sensitive<sup>47</sup> to  $\sigma$ . The decay rates that govern the evolution of  $\bar{f}(x, t)$  from  $t = 0$  to  $t = \infty$  are thus largely insensitive to the manner in which pitch-angle diffusion is distributed over  $x$ .

The approximation that  $T(y) \equiv T(1)$  in (5.01) causes the second term in that equation to vanish. This approximation is inappropriate for describing the temporal evolution of  $\bar{f}(x, t)$  near  $x \approx 1$  because the exact eigenfunctions of (5.01) are poorly approximated by (5.06a) for  $x \approx 1$ .

<sup>47</sup>For example, the quantity  $(1 - \sigma)\kappa_{v0}$  varies from 3.14 to 1.92 as  $\sigma$  goes from  $-1$  to  $+1/2$ . The ratio  $\lambda_1/\lambda_0$  varies from 9.0 to 3.4 over this same  $\sigma$  interval.

Without the approximation, the eigenvalue equation becomes [cf. (3.52b), Section III.8]

$$\lambda_n = -\frac{1}{x g_n} \frac{\partial}{\partial x} \left[ x D_{xx} \frac{\partial g_n}{\partial x} \right]_E + \frac{D_{xx}}{y} \frac{T'(y)}{T(y)} \left[ \frac{\partial \ln g_n}{\partial \ln x} \right]_E. \quad (5.07)$$

Since  $g_n(x_c) = 0$  and  $T'(y) < 0$  (see Section I.4), the second term of (5.07) is positive at  $x = x_c$ , i. e.,  $(\partial \ln g_n / \partial \ln x)_E < 0$  at  $x = x_c$ . Since the first term of (5.07) is also positive, the Bessel functions in the approximate solution (5.06a) approach zero more abruptly at  $x = x_c$  than do the true eigenfunctions. The discrepancy between (5.06a) and the true eigenfunctions grows with increasing  $x_c$ , since according to (1.28), the function  $T'(y) \approx -(1/4)[T(0) - T(1)](2 + y^{-1/2})$  approaches  $-\infty$  as  $x$  goes to unity (see Section I.4). A schematic illustration of the true eigenfunction  $g_0(x)$  and its Bessel-function approximation for  $\sigma = 0$  is given in Fig. 70 for each of three values of  $x_c$ .

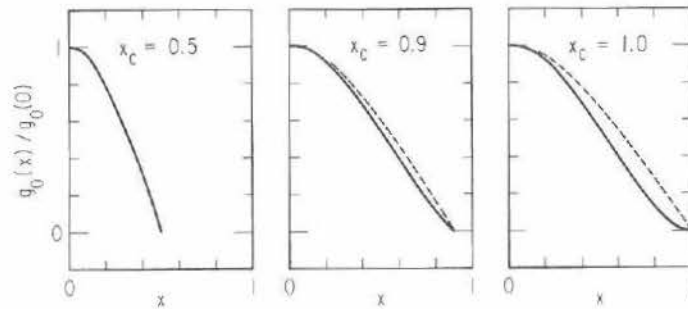


Fig. 70. Schematic representation of true eigenfunctions (solid curves) and approximate (Bessel) eigenfunctions (dashed curves) for lowest normal mode of pitch-angle diffusion with  $\sigma = 0$ .

The use of the true pitch-angle eigenfunctions  $g_n(x)$  is essential for extracting a radial-diffusion coefficient from low-altitude electron observations beyond  $L \approx 1.6$  (e. g., Fig. 36, Section IV.2). As shown in Section IV.2, the intensity of electrons on trajectories with "perigee"  $\lesssim 100$  km increases with longitude east of the South Atlantic "anomaly", as pitch angle diffusion replenishes the pitch-angle interval  $x_c < x < x_b$  (cf. Section II.7). This replenishment follows the sudden loss (by atmospheric absorption) of electrons with pitch angles  $x_c < x$  as they azimuthally drift through the "anomaly" region. In effect, the loss cone seen by the

electron distribution suddenly enlarges as the particles approach the "anomaly", where  $x_b = x_c$ . Immediately east of the "anomaly", fewer precipitating particles are observed than immediately west of the "anomaly", since no electrons remain in the loss cone. In other words, after the excess electrons are lost in the "anomaly", the pitch angle distribution vanishes at  $x = x_c$ .

A reasonable method of analyzing such electron observations to obtain  $D_{xx}$  is to assume that an isotropic source term  $S$  is distributed uniformly in longitude, as in (5.05). The addition of this source term to (5.01), together with the boundary condition that  $f(x, t)$  vanish for  $x = x_b(\varphi)$ , defines a straightforward problem of numerical analysis<sup>48</sup>. Any initial ( $t = 0$ ) choice of  $f(x, t)$  must evolve (for  $S \neq 0$ ) toward a periodic solution satisfying  $f(x, t + 2\pi/\Omega_3) = f(x, t)$ . The azimuthal coordinate  $\varphi$  of the particle distribution is a function of time in the sense that  $\dot{\varphi} = \Omega_3$ . (Recall that  $\Omega_3$  is approximately independent of  $x$  at a given energy and  $L$  value, cf. Section I.4.) The periodic solution  $f(x, t) = f(x, t - 2\pi/\Omega_3)$  obtained by following the particle distribution in its azimuthal drift is equivalent to a time-independent distribution  $f(x, \varphi)$ , where  $\varphi$  is the geomagnetic longitude. The functional form of  $f(x, \varphi)$  depends only upon  $D_{xx}/\Omega_3$  for a given  $x_b(\varphi)$ . Execution of the above-described computational program for many trial values of  $D_{xx}/\Omega_3$  should therefore yield one solution  $f(x, \varphi)$  that best agrees with observations (e. g., Fig. 36, Section IV.2). The observed azimuthal variation of  $\bar{f}(x, \varphi)$  thus yields a value of  $D_{xx}/\Omega_3$  and (since  $\Omega_3$  is a known function of  $E$  and  $L$ ) a value for  $D_{xx}$ .

The only reported computation of this nature [77] employed  $g_n(x) = (2/x^2)^{1/2} \cos[(2n+1)(\pi x/2x_b)]$  for the pitch-angle eigenfunctions. The results of that computation are therefore probably unreliable; sinusoidal eigenfunctions do not satisfy (5.01). The reported values for  $D_{xx}$  varied from  $2 \times 10^{-3} \text{ day}^{-1}$  at  $L = 2$  to  $8 \times 10^{-3} \text{ day}^{-1}$  at  $L = 4$ . The corresponding electron "lifetimes" ( $\approx 4/\pi^2 D_{xx}$ ) would amount to  $\sim 200$  days at  $L = 2$  and  $\sim 50$  days at  $L = 4$  for electron energy  $E \approx 0.6 \pm 0.2 \text{ MeV}$ . Since these "lifetimes" exceed those shown in Fig. 41 (Section IV.3) by nearly an order of magnitude, the numerical values of  $D_{xx}$  on which they are based are open to question. It is difficult, of course, to rule out a possible variation of  $D_{xx}$  with  $x$  or  $\varphi$  that might explain the

<sup>48</sup>Due to the South American anomaly (cf. Fig. 30, III.7) which lies immediately to the west, the loss cone expands abruptly from a small aperture ( $\cos^{-1} x_b$ ) to a larger aperture ( $\cos^{-1} x_c$ ) in the neighborhood of the South Atlantic "anomaly". It is mathematically convenient to model the loss-cone aperture as a step function of azimuth, rather than a sinusoidal function [cf. (2.75), Section II.8]. In fact, the step function may be the more faithful representation of geophysical reality.

discrepancy<sup>49</sup>, but a treatment based upon the true eigenfunctions of (5.01) is much needed.

Information on the possible energy dependence of  $D_{xx}$  east of the "anomaly" can be deduced by comparing the energy spectra of precipitating electrons at several longitudes  $\Delta\varphi$ , where  $\Delta\varphi=0$  at the "anomaly" [77]. Precipitating electrons having energies from 0.4 MeV to 2.5 MeV are found to have an exponential energy spectrum. The  $e$ -folding energy  $E_0$  is found to increase with increasing east longitude. This observation can be understood largely in terms of the energy-dependent azimuthal-drift rates (cf. Section I.4). Thus, the pitch-angle diffusion coefficient  $D_{xx}$  apparently is not a strong function of electron energy in the range  $E \approx 0.4$ –2.5 MeV.

### V.3 Quadrature (Spatial)

The diffusion equation can be manipulated in several ways in an attempt to extract the radial diffusion coefficient  $D_{LL}$  and/or the particle lifetime  $\tau$  from the observational data. One class of methods involves a partial integration of the diffusion equation between two fixed limits in  $L$  or time. Letting  $F \equiv \ln \bar{f}$  allows the radial diffusion equation [cf. (3.48), Section III.8] to be written as

$$\frac{\partial F}{\partial t} = \left[ L^2 \frac{\partial}{\partial L} \left( \frac{D_{LL}}{L^2} \right) \right] \frac{\partial F}{\partial L} + D_{LL} \left[ \frac{\partial^2 F}{\partial L^2} + \left( \frac{\partial F}{\partial L} \right)^2 \right] - \frac{1}{\tau} \quad (5.08)$$

for constant  $M$  and  $J$ . If the true lifetime  $\tau$  is a known function of  $L$ , and if  $F(L, t)$  is available from the observational data<sup>50</sup>, then (5.08) may be interpreted as a linear first-order differential equation for  $D_{LL}$ . If the observations of  $F$  cover the interval  $L_1 \lesssim L \lesssim L_2$ , then the solution of (5.08) may be written

<sup>49</sup>Enhanced pitch-angle diffusion subsequent (in longitude) to "complete" replenishment of the equatorial-pitch-angle-cosine interval  $x_c < x < x_b$  might escape detection by the above analytic method if it is accompanied by an enhanced source  $S$  [cf. (5.05)]. Any such enhancement of  $D_{xx}$  in longitude, however, should be correlated with magnetospheric longitude (local time) rather than geographic longitude, since atmospheric scattering of electrons is unimportant beyond  $L \approx 1.5$  (cf. Fig. 41, Section IV.3, and Figs. 72–73 below).

<sup>50</sup>Since only derivatives of  $F \equiv \ln \bar{f}$  appear in (5.08), the result is not affected by adding a constant to  $F$ . Thus, if the functional form of  $\bar{f}(L, t)$  is known, the absolute normalization is not required. Only the form of the flux profile at constant  $M$  and  $J$  affects (5.08).

$$D_{LL}(L) = \exp \left[ - \int_{L_3}^L Q_1(L) dL \right] \left\{ D_{LL}(L_3) + \int_{L_3}^L Q_2(L) \exp \left[ \int_{L_3}^L Q_1(L') dL' \right] dL \right\}, \quad (5.09a)$$

where

$$Q_1(L) = \left( \frac{\partial F}{\partial L} \right)^{-1} \left[ \frac{\partial^2 F}{\partial L^2} + \left( \frac{\partial F}{\partial L} \right)^2 - \frac{2}{L} \left( \frac{\partial F}{\partial L} \right) \right] \quad (5.09b)$$

$$Q_2(L) = \left( \frac{\partial F}{\partial L} \right)^{-1} \left[ \frac{\partial F}{\partial t} + \frac{1}{\tau} \right]. \quad (5.09c)$$

The value of  $L_3$  must lie within the range covered by the data, but is otherwise arbitrary. The value of  $D_{LL}$  at  $L=L_3$  plays the role of an arbitrary integration constant. The presence of an arbitrary constant, whose value must be estimated by other means, is a persistent difficulty of analytical methods in which  $D_{LL}$  is expressed as a spatial quadrature.

The use of  $F \equiv \ln \bar{f}$  rather than  $\bar{f}$  itself in (5.08) is advantageous from the computational standpoint. The standard use of finite-difference techniques in evaluating an expression like (5.09) tends to introduce far less error in the derivatives of  $F$  than in the derivatives of  $\bar{f}$ .

The method of (5.09) is clearly inapplicable, however, if  $\partial F/\partial L$  vanishes anywhere in the interval of interest ( $L_1 \leq L \leq L_2$ ). In such a case, it may be fruitful to return to (3.48), written in the form

$$\frac{\partial}{\partial L} \left[ \frac{D_{LL}}{L^2} \left( \frac{\partial \bar{f}}{\partial L} \right) \right]_{M, J} = \frac{1}{L^2} \left[ \frac{\bar{f}}{\tau} + \frac{\partial \bar{f}}{\partial t} \right]. \quad (5.10)$$

The full quadrature of (5.10) can be written as

$$D_{LL}(L) = L^2 \left( \frac{\partial \bar{f}}{\partial L} \right)^{-1} \int_{L_3}^L \left[ \frac{\bar{f}}{\tau} + \frac{\partial \bar{f}}{\partial t} \right] \frac{dL}{(L)^2} + \left[ \frac{D_{LL}}{L^2} \frac{\partial \bar{f}}{\partial L} \right]_{L=L_3} \\ = \frac{L^2}{\bar{f}} \left( \frac{\partial F}{\partial L} \right)^{-1} \int_{L_3}^L \left[ \frac{1}{\tau} + \frac{\partial F}{\partial t} \right] \frac{\bar{f} dL}{(L)^2} + \left[ \frac{D_{LL}}{L^2} \bar{f} \left( \frac{\partial F}{\partial L} \right) \right]_{L=L_3}. \quad (5.11)$$

Here the arbitrary integration constant  $D_{LL}(L_3)$  reappears. Now, however, if  $L_3$  is chosen so that  $\partial F/\partial L=0$  at  $L=L_3$ , then it follows from (5.11) that

$$D_{LL}(L) = \frac{L^2}{\bar{f}} \left( \frac{\partial F}{\partial L} \right)^{-1} \int_{L_3}^L \left[ \frac{1}{\tau} + \frac{\partial F}{\partial t} \right] \frac{\bar{f} dL}{(L)^2}. \quad (5.12)$$

Here, as in (5.09), the normalization of  $\bar{f}$  does not affect the value of  $D_{LL}$  extracted from the data by integrating to an  $L$  value of interest.

When it is impossible to choose  $L_3$  such that  $(\partial F/\partial L)_{L=L_3}$  vanishes, the difficulty associated with an arbitrary integration constant can often be circumvented by postulating the analytical form of  $D_{LL}$  a priori. The functional form customarily postulated (subject to later verification) is a power law in  $L$  (cf. Sections III.2 and III.3), i. e.,  $D_{LL} = D_n L^n$ . Under this assumption, it follows from (5.08) that

$$D_n = L^{-n} \left[ \frac{1}{\tau} + \frac{\partial F}{\partial t} \right] \div \left[ \left( \frac{n-2}{L} \right) \frac{\partial F}{\partial L} + \frac{\partial^2 F}{\partial L^2} + \left( \frac{\partial F}{\partial L} \right)^2 \right] \quad (5.13)$$

for some initially chosen value of  $n$  (not necessarily an integer). Since (5.13) follows from the assumption that  $D_{LL}$  is a "monomial" function of  $L$ , self-consistency can easily be checked by evaluating  $D_n$  from (5.13) for several values of  $L$  between  $L_1$  and  $L_2$ . A moderate scatter of the resulting  $D_n$  values about some constant mean would represent a measure of uncertainty in the numerical value of  $D_n$  while confirming the postulated power law. On the other hand, a systematic variation of  $D_n$  with  $L$  would indicate that  $n$  had been chosen improperly, i. e., that some other power law (or perhaps a different functional form altogether) is required in order that  $D_{LL}$  fit the data [113].

As indicated in Section IV.2, both the decay of inner-zone electron fluxes following the Starfish explosion (Fig. 32) and the decay of a monoenergetic electron enhancement observed after a magnetic storm (Fig. 35) have been adequately accounted for by atmospheric-scattering losses (Section II.2). Both sets of measurements had been made over a time interval that was relatively short compared to the calculated lifetimes. A long-term study of inner-zone electrons ( $E > 0.5$  MeV), covering a three-year period beginning in September 1962, revealed considerably longer *apparent* lifetimes in the region  $1.15 < L < 1.21$  than had been observed in the 50-day period immediately following the Starfish detonation. Since atmospheric scattering could not have grown abruptly less intense with time<sup>51</sup>, these measurements suggest that additional electrons were continually being supplied to these low  $L$  shells from higher  $L$ , perhaps by radial diffusion. An empirical analysis of these data for radial-diffusion effects is facilitated by the fact that the omnidirectional flux (profile shown in Fig. 71a) decayed almost exponentially during the three-year period that began in September 1962. The *apparent* decay rate  $-\partial F/\partial t$  and the decay rate  $1/\tau$  "expected" on the basis of atmospheric collisions (Section II.2) are shown in Fig. 71b [114].

<sup>51</sup>However, this was a period of decreasing solar activity (see Fig. 51, Section IV.5), during which the atmosphere would have contracted toward the earth.

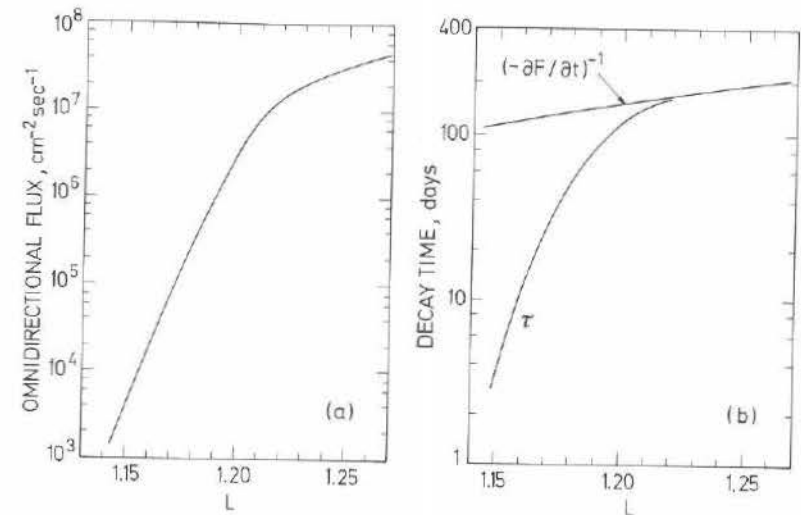


Fig. 71. (a) Inner-zone equatorial electron-flux profile for  $E > 1.6$  MeV observed on 1964-45A during December 1964; (b) decay times  $\tau$  and  $(-\partial F/\partial t)^{-1}$  derived from atmospheric-scattering theory [42] and from a three-year compilation [123] of inner-zone electron data (1962-65;  $E > 0.5$  MeV), respectively [114].

The "staircase" function shown in Fig. 72 represents a self-inconsistent determination of  $D_{LL}$  based on a hybrid analytical method [114] with features of both (5.12) and (5.13). The integral omnidirectional fluxes  $I_{4\pi}$  are first converted to equatorial differential unidirectional fluxes at constant  $M$  by postulating an energy spectrum like that which results from the beta decay of fission products (cf. Section V.6) and a pitch-angle distribution compatible with the known loss-cone aperture (cf. Section II.7). The pitch-angle correction (factor converting omnidirectional flux to unidirectional flux) varies by  $\sim 30\%$  between  $L = 1.15$  and  $L = 1.21$ ; it tends to reduce the slope of the flux profile. The conversion from  $I_{4\pi}$  at constant  $E$  to  $\bar{f} = J_{\perp}/p^2$  at constant  $M$  leads to a correction that varies by  $\sim 10\%$  over the interval  $1.15 < L < 1.21$ ; this correction tends to steepen the profile. The net result is that the profile  $\bar{f}$  is  $\sim 20\%$  less steep than that of  $I_{4\pi}$ , shown in Fig. 71a.

An acceptable procedure for obtaining  $D_{LL}$  from these observational data consists of replacing  $D_{LL}(L_3)$  on the right-hand side of (5.11) by  $(L_3/L)^n D_{LL}(L)$ . This is equivalent to assuming that  $D_{LL} \propto L^n$ . A rearrangement of terms then yields

$$D_{LL}(L_4) = \int_{L_3}^{L_4} \left[ \frac{1}{\tau} + \frac{\partial F}{\partial t} \right] \frac{\bar{f} dL}{(L)^2} \div \left[ \frac{\bar{f}}{L^2} \left( \frac{L}{L_4} \right)^n \frac{\partial F}{\partial L} \right]_{L=L_3}^{L=L_4} \quad (5.14)$$

In particular, the choice  $n=0$  corresponds to a diffusion coefficient  $D_{LL}$  that is constant in the interval  $L_3 \leq L \leq L_4$ . The "staircase" function shown in Fig. 72 results from performing the integral in (5.14) over a sequence of consecutive, adjacent  $L$  intervals of width  $L_4 - L_3 = 0.01$  for  $n=0$ . An alternative choice of intervals, such that  $L_4 - L_3 = 0.005$  yields very similar results, as does the use of (5.13) for  $n=0$ .

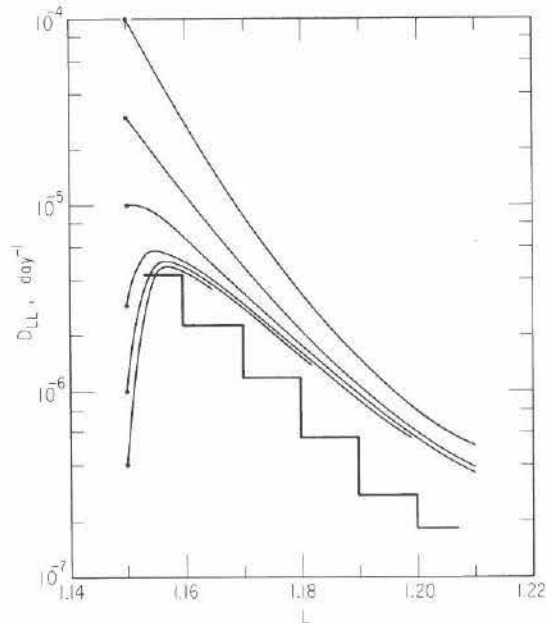


Fig. 72. Radial diffusion coefficients obtained from data in Fig. 73, assuming fission spectrum to obtain  $\bar{f}(M, J, \Phi)$  at constant  $M$  and  $J$ . Staircase function [114] follows from self-inconsistent quadrature. Smooth curves are self-consistent, but require assignment of arbitrary values (filled circles) to  $D_{LL}$  at  $L=1.15$  [115].

The inconsistency of the "staircase" function as a solution for  $D_{LL}$  is that the initial assumption ( $n=0$ ) has led to the conclusion that  $D_{LL}$  varies inversely as  $\sim L^{70}$ , *i.e.*, by a factor  $\sim 20$  between  $L=1.20$  and  $L=1.15$ . In fact, a treatment of the same data using (5.13) with  $n=-70$  proves to be reasonably self-consistent, and leads to a value of  $D_{LL}$  that is approximately twice as large as the "staircase" function at the center of each integration interval.

The alternative procedure of assigning  $D_{LL}$  a certain arbitrary value at  $L_3 = L_1 = 1.15$  yields the family of smooth curves shown in Fig. 72 [115]. Values of  $D_{LL}$  ranging from  $4 \times 10^{-7} \text{ day}^{-1}$  to  $3 \times 10^{-5} \text{ day}^{-1}$

arbitrarily assigned at  $L=1.15$  thus yield remarkably similar solutions for  $D_{LL}$  beyond  $L=1.17$ . The solution generated by  $D_{LL}(1.15) = 1.5 \times 10^{-5} \text{ day}^{-1}$  (not shown in Fig. 72) roughly approximates the above-described power law in magnitude and functional form. Of course, arbitrarily large values of  $D_{LL}(L)$  could be generated for  $L > L_1$  by an unreasonable choice of  $D_{LL}(L_1)$ .

Although the various operations on the data yield different solutions for  $D_{LL}$ , all solutions support the major conclusion that  $\partial D_{LL}/\partial L < 0$  for  $1.16 < L < 1.21$ . This is an interesting reversal of the trend evident in observations made beyond  $L=2$  (*cf.* Section IV.6), where  $D_{LL}$  appears to vary as a large ( $\sim 10$ ) positive power of  $L$ . The reversal perhaps originates from ionospheric-current impulses [114], but a variation so extreme ( $D_{LL} \propto L^{-70}$ ) would require very localized current distributions (spherical-harmonic number  $\sim 40$ ).

Another possible origin of the reversal is atmospheric pitch-angle scattering in the presence of shell splitting caused by internal geomagnetic multipoles (Fig. 30, Section III.7). It is apparent that  $D_{xx}$  has a strongly inverse variation with  $L$  (*cf.* Fig. 71b, the curve for  $1/\tau$ ). The analysis of Fig. 71 for such a constant-energy process must be based on (3.42), Section III.7, rather than on (3.48), since (3.48) applies to a constant- $M$  process. The term  $[(n-2)/L](\partial F/\partial L)$  in (5.13) must therefore be changed to  $[(n+2)/L](\partial F/\partial L)$ , for example. A somewhat larger magnitude of  $D_{LL}$  is required to account for the observations if a constant- $E$  process is postulated instead of a constant- $M$  process. As a rough estimate, the solutions for  $D_{LL}$  in Fig. 72 should be multiplied by a factor  $\sim 2$  in order to accommodate a process for which inward radial diffusion does not change a particle's energy.

As noted above, the appearance of an arbitrary integration constant  $D_{LL}(L_3)$  in (5.11) follows from the fact that  $\partial F/\partial L$ , as given by the data, fails to pass through zero in the interval  $1.15 < L < 1.21$  used for analysis. The region of  $L$  over which the inner electron belt is analyzed, therefore, might profitably be extended to  $L \approx 1.6$  so as to include the maximum in  $F$  that exists near  $L=1.4$  (see Fig. 73a)<sup>52</sup>.

The apparent decay rates  $-\partial F/\partial t$  are obtained from measurements made on the OV1-2 satellite, and are shown in Fig. 73b together with the calculated atmospheric-scattering lifetimes. The single point  $L \approx 1.77$  in the figure is the decay lifetime of the narrow electron belt created by the Soviet nuclear detonation of 1 November 1962 (see

<sup>52</sup>These electron "distribution functions" correspond to two different values of the first invariant  $M$  [116]. Since (5.08)–(5.14) do not explicitly couple distinct values of  $M$  by differential operators, it is permissible to plot  $L^3 J_{\perp}$  rather than  $J_{\perp}/MB$ . The calculations are unaffected by this choice.

Fig. 58, Section IV.6). The dashed curve in Fig. 73 b is an "interpolation" between observed pitch-angle diffusion lifetimes of inner-belt electrons. The function  $D_{LL}(L)$  obtained from (5.12) by using the lifetime data of Fig. 73 b for  $M=21.4$  MeV/gauss ( $E=1$  MeV at  $L=1.65$ ) is plotted in Fig. 73 b [116]. The value of  $D_{LL}$  at  $L=1.20$ , as obtained from these data, is two orders of magnitude larger than the value of  $D_{LL}$  at  $L=1.20$  shown in Fig. 72. The derived magnitude of  $D_{LL}$ , however, is fairly sensitive to the numerical value assigned to  $\tau$  at  $L=1.42$ . According to Fig. 41 (Section IV.3), this value should have been  $\sim 300$  days, which is much closer to the apparent lifetime  $-(\partial F/\partial t)^{-1}$  than the value of  $\tau$  actually used for the computation (dashed curve, Fig. 73 b).

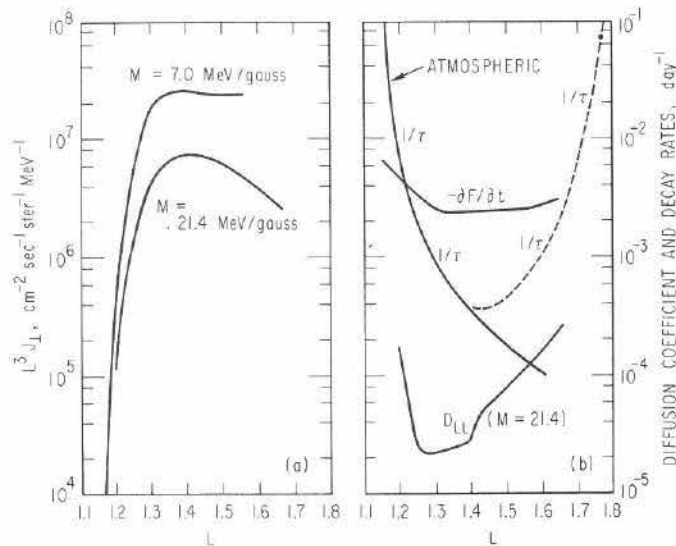


Fig. 73. (a) Profiles of electron distribution function ( $\times 2m_0 MB_0$ ) for  $J=0$ , based on OV1-2 data; (b) decay rates  $1/\tau$  expected from atmospheric scattering (solid curve) and wave-particle interaction (data point at  $L \approx 1.77$ ); (b) arbitrary interpolation (dashed curve); (b) decay rate  $(-\partial F/\partial t)$  actually observed for  $E > 0.5$  MeV; (b) diffusion coefficient  $D_{LL}$  derived from these data for  $M=21.4$  MeV/gauss [116].

The methods of this section are applicable not only to static profiles ( $\partial F/\partial t=0$ ) but also to time-varying profiles ( $\partial F/\partial t \neq 0$ ). The methods can easily be modified to include the effects of a distributed source [e.g., (3.57), Section III.8], as well as particle deceleration without pitch-angle diffusion. It is probably unwise, however, to attempt a purely

spatial quadrature on the observed distribution of outer-zone electron fluxes. This reservation holds because outer-zone electron fluxes exhibit considerable fluctuation with time, rather than a slow evolution of the profile. Much of the observed variation is not related to radial diffusion in a simple way (cf. Sections IV.6 and IV.8). Even when special care is taken to select only geomagnetically quiet time intervals, the methods of this section are found to yield unreasonably large magnitudes and dubious functional forms for  $D_{LL}$  [117].

#### V.4 Quadrature (Temporal)

In the presence of temporal fluctuations such as those commonly observed in outer-zone electron fluxes, it is essential not only to select carefully the time interval chosen for analysis, but also to evaluate time derivatives of  $F$  from several-day averages. The interval chosen for analysis must be free of large "injection" events (cf. Fig. 38, Section IV.3) characterized by *in situ* particle energization, as such processes cannot easily be included in the diffusion equation. Other temporal changes in the particle fluxes, such as those due to field changes on both the adiabatic and impulsive time scales, must be averaged over time to avoid spurious contributions to  $\partial F/\partial t$ .

Care must be taken in obtaining the average of  $\partial F/\partial t$  over several days, however, since outer-zone electron lifetimes are typically 5–10 days (cf. Fig. 41, Section IV.3). Thus, the averaging procedure must be sophisticated enough to accommodate the true evolution of  $F(L, t)$  during the several-day time interval over which the average is taken. One procedure for performing this average, sometimes termed the *temporal quadrature* of (5.08), involves the assumption (cf. Section V.3) that  $D_{LL} \propto L^n$ . If  $D_n$  and  $\tau$  are regarded as time-independent during the interval  $t_1 \leq t \leq t_2$ , then it follows from (5.08) that

$$D_{LL} \equiv D_n L^n = \{F(t_2) - F(t_1) + [(t_2 - t_1)/\tau]\} \div \int_{t_1}^{t_2} \left[ \left( \frac{n-2}{L} \right) \frac{\partial F}{\partial L} + \frac{\partial^2 F}{\partial L^2} + \left( \frac{\partial F}{\partial L} \right)^2 \right] dt. \quad (5.15)$$

The diffusion coefficient  $D_{LL}$  can thus be determined from electron data such as those shown in Fig. 74 [93]. These data have been converted to equivalent equatorial profiles of  $L^3 J_{\perp}$  ( $\equiv 2m_0 MB_0 \bar{f}$ ) at constant  $M$  (cf. Fig. 54, Section IV.6). By choosing  $t_1$  and  $t_2$  appropriately, so that  $F(t_2) \gtrsim F(t_1)$ , it might be possible to estimate  $D_n$  for each assigned

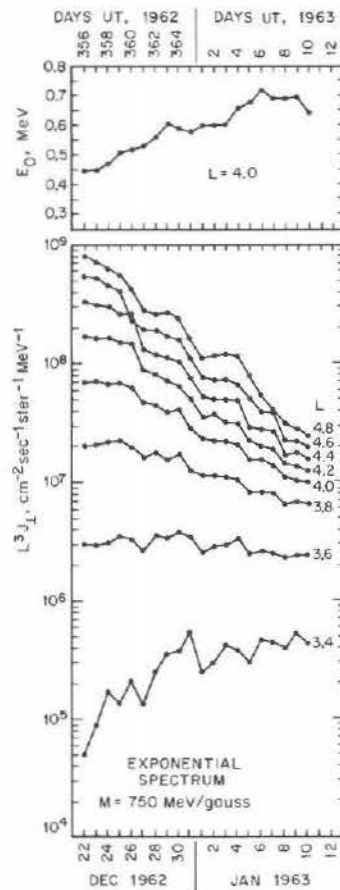


Fig. 74. Evolution of equatorial daily-median  $L^3 J_{\perp}$  and spectral parameter following magnetic storm of 17 December 1962 [93], based on Explorer-15 electron data (cf. Figs. 53 and 54).

$n$ . The "best" value of  $n$  would be that for which  $D_n$  is most nearly independent of  $L$  (cf. Section V.3).

Unfortunately, the application of (5.15) to the full twenty-day interval of data shown in Fig. 74 does not allow a precise determination of  $D_{LL}$ . This is because the quantity  $F(t_2) - F(t_1)$  is negative at each  $L$  value shown (as is usual for such a long time interval) and represents a good approximation for  $(t_1 - t_2)/\tau$ . The numerator of (5.15) is therefore approximately zero, and so is very sensitive to the somewhat arbitrary choice of lifetime  $\tau(L)$ . This difficulty arises quite frequently in practice,

since (as noted above)  $t_2 - t_1$  must be chosen sufficiently long to average out the adiabatic fluctuations<sup>53</sup> in  $\partial F/\partial t$ .

An alternative to the above procedure is to solve (5.15) for the pitch-angle-diffusion lifetime  $\tau(L)$ , in terms of the radial diffusion coefficient  $D_{LL} = D_n L^n$ . In this case, time-independent values of  $n$  and  $D_n$  are chosen somewhat arbitrarily in order to obtain

$$\frac{1}{\tau} = \frac{D_n L^n}{t_2 - t_1} \int_{t_1}^{t_2} \left[ \left( \frac{n-2}{L} \right) \frac{\partial F}{\partial L} + \frac{\partial^2 F}{\partial L^2} + \left( \frac{\partial F}{\partial L} \right)^2 \right] dt - \frac{F(t_2) - F(t_1)}{t_2 - t_1}. \quad (5.16)$$

For use in (5.16) the observational data shown in Fig. 74 can be manipulated to yield numerical derivatives given by the algebraic expressions  $F'(L;t) = (5/2)[F(L+0.2;t) - F(L-0.2;t)]$ ,  $F''(L;t) = 25[F(L+0.2;t) - 2F(L;t) + F(L-0.2;t)]$  and  $\dot{F}(L,t) = (1/2)[F(L;t+1) - F(L;t-1)]$ ,

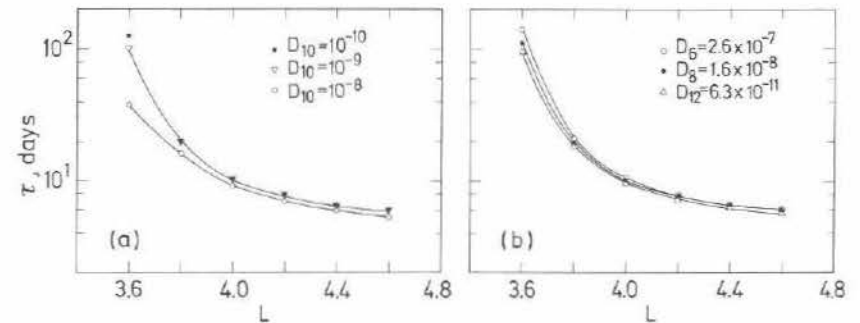


Fig. 75. Electron lifetimes ( $M=750$  MeV/gauss) obtained from data of Fig. 74 by using (5.16) for selected values of  $D_n$  day<sup>-1</sup>.

with time  $t$  measured in days. Numerical integration of (5.16) by Simpson's rule then yields the lifetimes shown in Fig. 75a.

<sup>53</sup>The fluctuations superimposed on the mean evolution in Fig. 74 are found to be well correlated with the ring-current index  $D_{SI}$  (cf. Section I.5). However, attempts to suppress these apparently adiabatic fluctuations by means of a ring-current model (cf. Fig. 9, Section I.5) and available spatial and spectral information (cf. Fig. 43, Section IV.3) did not succeed for the data of Fig. 74. Perhaps the modeling procedures commonly used for protons (Fig. 43) are insufficiently accurate to subtract the adiabatic fluctuations of outer-zone electrons with confidence.

The functions  $\tau(L)$  shown in Fig. 75a are very similar, although the inserted values of  $D_{10}$  vary over two orders of magnitude. The choice of  $n=10$  follows a convention based on "theoretical" considerations (cf. Sections III.2, III.3, and III.8). Since all choices from  $10^{-10}$  day $^{-1}$  to  $10^{-8}$  day $^{-1}$  for the magnitude of  $D_{10}$  are found to yield equally reasonable lifetime functions  $\tau(L)$ , the "correct" magnitude for  $D_{10}$  must be obtained by invoking some further empirical consideration.

Values of  $n \neq 10$  yield similar  $\tau(L)$  functions to those shown in Fig. 75a if  $D_n$  is chosen appropriately. Since the observations cover a range centered at  $L \approx 4$ , a logical comparison among different values of  $n$  would require that  $D_n 4^n$  be held fixed. Thus, the  $\tau(L)$  functions plotted in Fig. 75b for  $n=6, 8,$  and  $12$  (with  $D_n = D_{10} 4^{10-n}$ ) are virtually indistinguishable.

If the data of Fig. 74 are analyzed in blocks of five days instead of twenty, (i. e.,  $t_2 - t_1 = 5$  days) the application of (5.16) to these separate intervals is found to yield lifetime functions  $\tau(L)$  that duplicate Fig. 75 within a factor of two. Thus, while temporal quadrature yields self-consistent lifetimes against pitch-angle diffusion, the extraction of a radial-diffusion coefficient  $D_{LL}$  from data such as shown in Fig. 74 apparently requires another (more sophisticated) analytical technique.

## V.5 Variational Method

A major disadvantage of quadrature (either spatial or temporal, cf. Sections V.3 and V.4) in the extraction of transport coefficients from time-varying electron data is that either  $D_{LL}$  or  $D_{xx}$  must be given *a priori* in order to obtain the other. An empirical technique termed the "variational method" circumvents this difficulty and thus enables both the radial-diffusion coefficient  $D_{LL}$  and the particle-lifetime function  $\tau(L)$  to be extracted simultaneously from the data with minimum reliance on *ad hoc* assumptions about the  $L$  dependence of  $\tau$ .

The variational technique involves the usual tacit assumptions that both  $\tau$  and  $D_{LL}$  are time-independent and that  $D_{LL}$  can be represented in the form  $D_{LL} = D_n L^n$ . Then the temporal evolution of  $F(L, t)$ , as given by (5.08), can be attributed to a combination of diffusion across  $L$  and pitch-angle scattering into the loss cone. To the extent that radial diffusion can be accounted for by properly choosing the magnitude and functional form of  $D_{LL}$ , the remaining temporal decay of  $F$  via pitch-angle scattering should be linear, corresponding to an exponential decay of  $\bar{f}(L, t)$ . The idea of the variational method [93] is to formulate a quantitative measure of the extent to which a given  $D_n$  "fails" to

account for the nonlinear temporal component of the evolution of  $F(L, t)$ .

This formulation is facilitated by introducing the decay-rate function [cf. (5.16), Section V.4]

$$\lambda_n(L, t) \equiv D_n L^n \left[ \left( \frac{n-2}{L} \right) \frac{\partial F}{\partial L} + \frac{\partial^2 F}{\partial L^2} + \left( \frac{\partial F}{\partial L} \right)^2 \right] - \frac{\partial F}{\partial t}. \quad (5.17)$$

This function reduces to a constant in time [viz.,  $1/\tau(L)$ ] only if  $F(L, t)$ , as given by the data, exactly satisfies (5.08). The "correct" value of  $n$  is that which enables  $D_n$  to be chosen so that  $\lambda_n(L, t)$  is constant in time, and the "correct" value of  $D_n$  is that which makes  $(\partial \lambda_n / \partial t)_L$  vanish.

In practice, of course, there will be uncertainties in the data, and it may be impossible to suppress adiabatic fluctuations satisfactorily (cf. Section V.4). These and other difficulties prevent  $\lambda_n(L, t)$ , as given by the data, from being *exactly* constant in time under any conditions. It is possible, however, to ask (for any given  $n$ ) that  $D_n$  be chosen so that  $\lambda_n(L, t)$  deviates *minimally* from a constant. The deviation of  $\lambda_n(L, t)$  from a constant in time can be expressed quantitatively by introducing a function

$$G_n(D_n) \equiv \int_{L_1}^{L_2} g(L) \int_{t_1}^{t_2} [\lambda_n^2 - \langle \lambda_n \rangle^2] dt dL, \quad (5.18)$$

where  $\langle \lambda_n \rangle$  is the temporal mean value of  $\lambda_n(L, t)$  and  $g(L)$  is a positive-definite weighting function<sup>54</sup>. The function  $G_n(D_n)$  is thus a quantitative measure of the "failure" of a specific numerical value of  $D_n$  to account for the time variation of  $F$  attributable to radial diffusion. The function  $G_n(D_n)$  is minimized with respect to its argument ( $D_n$ ) by requiring that

$$\frac{\partial G_n}{\partial D_n} = 2 \int_{L_1}^{L_2} g(L) \int_{t_1}^{t_2} \left[ \lambda_n \frac{\partial \lambda_n}{\partial D_n} - \langle \lambda_n \rangle \frac{\partial \langle \lambda_n \rangle}{\partial D_n} \right] dt dL = 0. \quad (5.19)$$

This linear algebraic equation for  $D_n$  yields a numerical value of  $D_n$  that is uniquely determined by the data for a given weighting function  $g(L)$ . The optimal ( $G_n$ -minimizing) value of  $D_n$  is given by

<sup>54</sup>The purpose of  $g(L)$  is to distribute responsibility for the ultimate determination of  $D_n$  equitably among the various  $L$  values (see below).

$$\begin{aligned}
 D_n = & \int_{L_1}^{L_2} L^n g(L) \int_{t_1}^{t_2} \left\{ \frac{\partial F}{\partial t} \left[ \left( \frac{n-2}{L} \right) \frac{\partial F}{\partial L} + \frac{\partial^2 F}{\partial L^2} + \left( \frac{\partial F}{\partial L} \right)^2 \right] \right. \\
 & \left. - \left[ \frac{F(t_2) - F(t_1)}{t_2 - t_1} \right] \left\langle \left( \frac{n-2}{L} \right) \frac{\partial F}{\partial L} + \frac{\partial^2 F}{\partial L^2} + \left( \frac{\partial F}{\partial L} \right)^2 \right\rangle \right\} dt dL \\
 & \div \int_{L_1}^{L_2} L^{2n} g(L) \int_{t_1}^{t_2} \left\{ \left[ \left( \frac{n-2}{L} \right) \frac{\partial F}{\partial L} + \frac{\partial^2 F}{\partial L^2} + \left( \frac{\partial F}{\partial L} \right)^2 \right]^2 \right. \\
 & \left. - \left\langle \left( \frac{n-2}{L} \right) \frac{\partial F}{\partial L} + \frac{\partial^2 F}{\partial L^2} + \left( \frac{\partial F}{\partial L} \right)^2 \right\rangle^2 \right\} dt dL, \tag{5.20}
 \end{aligned}$$

where the angle brackets denote a time average over the interval  $t_1 \leq t \leq t_2$ . The calculation of an optimal  $D_n$  by (5.20) can be carried out for each of many values of  $n$ . Insertion of the optimal  $D_n$  in (5.16) allows a determination of the decay constant  $1/\tau(L) \equiv \langle \lambda_n(L, t) \rangle$ . The best-fitting functional form of  $D_{LL} = D_n L^n$  can perhaps be identified by searching for an absolute minimum in  $G_n(D_n)$  among the various values of  $n$ . If some  $n$  is clearly identified as the optimum, the corresponding  $\langle \lambda_n(L, t) \rangle^{-1}$  is simultaneously established (although tentatively, cf. Section V.6) as the optimum lifetime function  $\tau(L)$ . In practice [93], many values of  $n$  yield almost identical minima in  $G_n(D_n)$ . The optimal value of  $D_n$  is thus identified for each  $n$ , but the best value of  $n$  remains unidentified (cf. Section V.4).

The data of Fig. 74 (Section V.4) were extracted from flux profiles such as those in Fig. 53 (Section IV.6) by assuming an exponential energy spectrum at each  $L$  value. Very similar data representing  $L^3 J_{\perp} = 2m_0 M B_0 \bar{j}$  are obtained by postulating a power-law spectrum

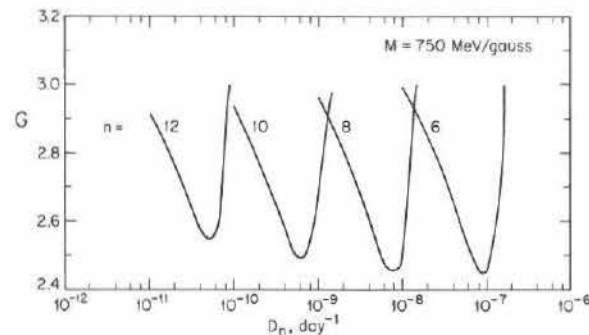


Fig. 76. Functions  $G_n(D_n)$  obtained for  $g(L) \equiv 1$ , from data similar to those of Fig. 74 but using a power-law spectrum (cf. Fig. 54) for energy interpolation [93].

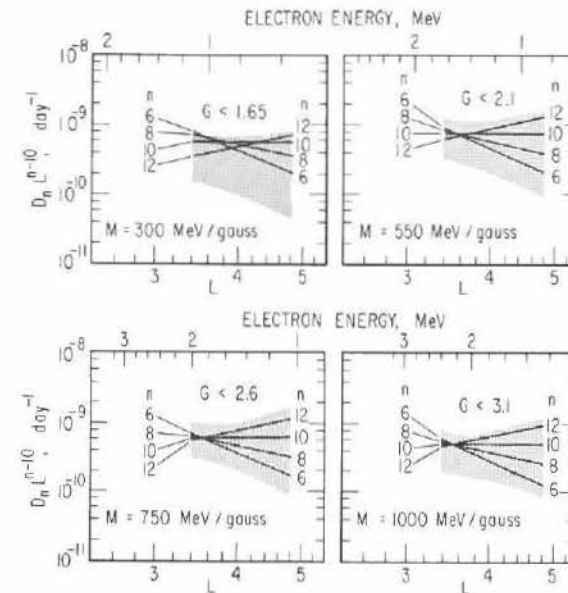


Fig. 77. Optimal values (solid lines) of  $L^{-10} D_{LL}$  obtained by variational method, with  $g(L) \equiv 1$ , from data of Fig. 74. Shaded area represents range of values acceptable [93] in the context of Fig. 76.

for interpolation between  $E=0.5$  MeV and  $E=1.9$  MeV (cf. Fig. 53 [93]). The functions  $G_n(D_n)$  constructed [using (5.18)] from these power-law data are plotted in Fig. 76 for several values of  $n$  with  $g(L) \equiv 1$ . It is evident from Fig. 76 that the optimal ( $G_n$ -minimizing) value of  $D_n$  is easily identified for any given  $n$ . On the other hand, the several values of  $n$  yield virtually identical minimum values for the functions  $G_n(D_n)$ . The failure of the variational method to yield a unique optimum value of  $n$  in this case is perhaps a consequence of the narrowness of the interval in  $L$  available for analysis ( $L_2 - L_1 = 1.4$ ;  $L_2/L_1 = 1.4$ ).

The optimal values of  $D_n L^{n-10}$  obtained from the analyses [cf. (5.20)] for several values of  $n$  and four values of  $M$  are shown in Fig. 77 by solid lines. The shaded area contains all values of  $D_{LL}/L^{10}$  such that  $6 \leq n \leq 12$  and  $G_n(D_n)$  is less than the stated limit (e.g.,  $G_n < 2.6$  at  $M=750$  MeV/gauss). The several values of  $n$  thus yield a fairly consistent value of  $D_{LL}$  at  $L \approx 3.6$  (cf. Section V.4). The lifetime functions  $\tau(L)$  are obtained for each  $M$  by inserting in (5.16) the optimal values of  $D_n$ , as obtained from (5.20). The results are shown in Fig. 78 [93].

The variational method is a good technique for extracting numerical values of the transport coefficients  $D_{LL}$  and  $\tau$  from observational data

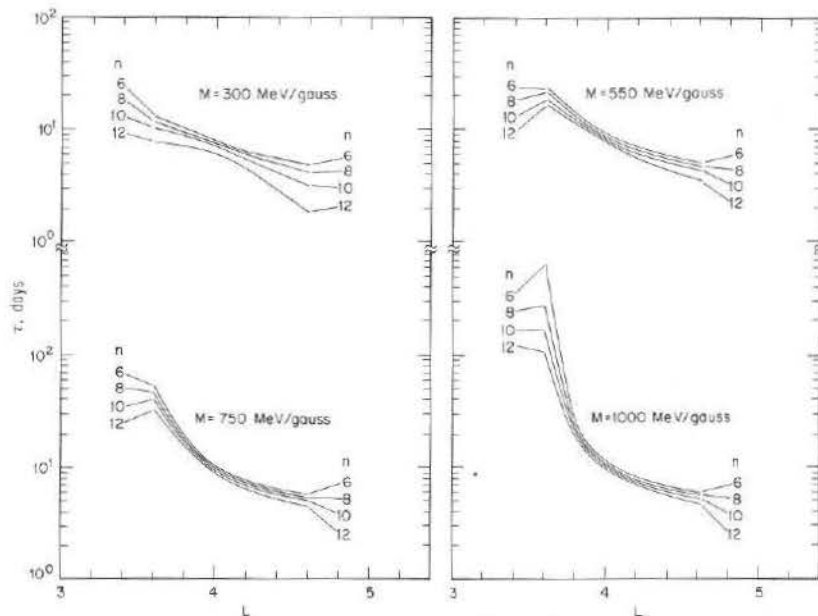


Fig. 78. Electron lifetimes obtained from (5.16) by inserting optimal values of  $D_n$  indicated in Fig. 77 [93].

consisting of time-varying flux profiles<sup>55</sup>. When used in conjunction with one of the verifying methods described below (Section V.6), the variational method constitutes a systematic and expedient means of analyzing the observational data for simultaneous radial and pitch-angle diffusion.

Certain refinements of the variational method merit further attention. Since  $\langle \lambda_n(L, t) \rangle$  is found to vary by an order of magnitude between  $L=3.6$  and  $L=4.6$  (cf. Figs. 75 and 78), use of the weighting function  $g(L) \equiv 1$  in (5.18) tends to leave  $G_n(D_n)$  relatively insensitive to observations made at  $L \lesssim 4$ . Thus, in identifying the optimal value of  $D_n$ , undue weight is perhaps assigned to the region  $L \gtrsim 4$ . An alternative weighting function of the form  $g(L) \equiv 65/L^3$ , normalized to a unit mean value in the interval  $3.4 < L < 4.8$ , partially redresses the imbalance and introduces no significant change in Figs. 76–78 [93]. However, a weighting function that more fully compensates for the  $L$  dependence of  $\tau$  might be more suitable.

The variational method is potentially sensitive to genuine temporal variations of the transport coefficients  $D_{LL}$  and  $\tau$ . There is no provision

<sup>55</sup>Note that (5.20) is indeterminate for any time interval  $t_1 \leq t \leq t_2$  in which  $\partial F / \partial t = 0$ .

in (5.18)–(5.20) for recognizing such variations. Moreover, if the data are rather “noisy” as in Fig. 74, containing fluctuations unrelated to radial and pitch-angle diffusion, the equations may seek to minimize  $G_n(D_n)$  not by selecting the best  $D_{LL}$  and  $\langle \lambda_n(L, t) \rangle$ , but by selecting unrealistically small values of  $\langle \lambda_n(L, t) \rangle$ . Such a selection would also tend to underestimate the magnitude of  $D_{LL}$  appropriate for (5.08). For these and other reasons, the magnitudes of  $D_{LL}$  and  $\tau(L)$  that follow from (5.20) and (5.16), respectively, should be regarded as tentative choices. It remains to verify that, when these numerical values are inserted into (5.08), the actual evolution of  $F(L, t)$  is correctly predicted by integrating this diffusion equation with respect to time (cf. Section V.6).

## V.6 Temporal Integration

As described in the previous section, estimates of the radial and pitch-angle diffusion coefficients can be extracted from observed time variations in the electron fluxes. Verification of any proposed set of numerical values for  $D_{LL}$  and  $\tau(L)$ , whether obtained from the variational method or otherwise, requires that (5.08), the diffusion equation, be integrated with respect to time, using appropriately selected boundary conditions on  $F(L, t)$ . Initial conditions are determined, as far as possible, from the observational data. Given the initial and boundary conditions, the diffusion equation can then be integrated with respect to time. The result of this integration should be compared to the observed evolution of  $F(L, t)$ . Source terms are generally omitted for outer-zone electrons, since the observed variations in flux are presumed to occur after the source that produced the initial flux enhancement is turned off.

The inward-moving “edge” of the flux profile shown in Fig. 52a, Section IV.6 (from the same time period as the data in Fig. 74 treated above; see Sections V.4 and V.5), can be studied further by integrating (5.08), the diffusion equation, for  $F(L, t)$ . Since the observations consist of flux measurements for one energy threshold only, it is necessary to introduce assumptions as to the shape of the electron energy spectrum at  $t=0$  (20 December). In order to obtain  $F(L, 0)$  at constant first invariant  $M$ , the initial energy spectrum is assumed to be exponential (with an  $e$ -folding energy of 600 keV) at  $L=4$  (cf. Fig. 74, Section V.4), and consistent with (4.01), Section IV.5, at other  $L$  values.

The boundary conditions used in one analysis of these data are specified by extrapolating the  $t=0$  distribution function smoothly to zero at  $L=1$  and  $L=8$ . These boundary conditions are maintained throughout the computation. The decay time for electrons is taken

as a constant, equal to 20 days, independent of time,  $L$ , and  $M$ . The  $M$ -independent radial diffusion coefficient is assumed to be independent of time also (as in the variational approach) and to have an  $L^n$  power-law dependence. The integration of (5.08), using the above-specified spectrum, boundary conditions, and lifetimes, is performed by standard finite-difference techniques. The results for  $F(L,t)$  are then converted back to integral omnidirectional fluxes ( $E > 1.6$  MeV) for comparison with the observational data.

Results of the computation for each of two different values of  $D_{LL}$  are compared to the observational data in Fig. 79 [70]. It is difficult

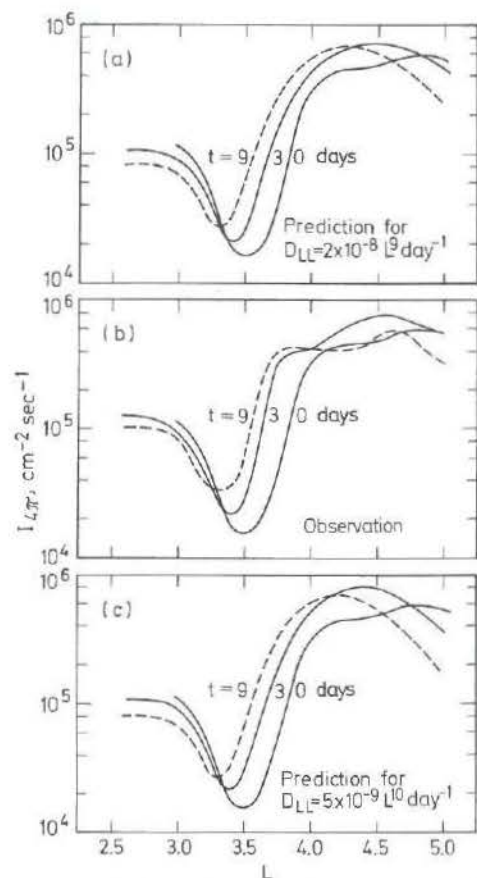


Fig. 79. Equatorial omnidirectional-flux profiles for electrons having  $E > 1.6$  MeV: (a, c) predictions generated by numerical integration from  $t=0$  (20 December 1962) for  $\tau=20$  days and  $D_{LL}$  as indicated, using fixed boundary conditions ( $\bar{f}=0$ ) at  $L=1$  and  $L=8$  [70]; (b) observations based on Explorer-14 data, shown also in Fig. 52a [111].

to choose the "better"  $D_{LL}$  from this comparison, but the slopes of the "leading edges" of the observed and calculated flux profiles possibly agree better for  $n=10$  than for  $n=9$ . Given the *ad hoc* assumptions, the agreement is found to be much poorer for other values of  $D_n$  and for other integer values of  $n$ . The two "best" diffusion coefficients  $D_{LL}$  agree in magnitude at  $L \approx 4$  (cf. Section V.4).

The validity of the results obtained by this method can presumably be tested by studying the sensitivity of these results to changes in the assumed initial conditions, boundary conditions, and lifetimes. Reasonable changes in the boundary conditions at  $L > 5$  (but not at  $L < 2.6$ ) are found to produce significant modifications in the results, but only in the region  $L > 4$  (not in the "leading-edge" region). The use of an initial  $e$ -folding energy of 400 keV or 800 keV, rather than 600 keV, at  $L=4$  is found to cause significant changes in the calculated fluxes at  $L$  values beyond the "leading edge" of the profile, but this does not alter the overall time evolution. The optimum radial diffusion coefficient, as obtained by this integration scheme, is  $D_{LL} \approx 5 \times 10^{-9} L^{10} \text{ day}^{-1}$ , a result that is largely insensitive to minor variations in the multitude of qualifying assumptions indicated.

A similar analysis can be made using measurements of the artificially produced "spike" of electron flux shown in Fig. 58 (Section IV.6). In this case, the initial flux distribution is taken as an approximate Gaussian in  $L$ , with boundary conditions selected such that the fluxes are held equal to zero at  $L=1.6$  and  $L=1.9$ . In order to obtain a constant- $M$  distribution function  $\bar{f} \equiv \exp F$ , the energy spectrum is assumed to have the form [118]

$$J_{\perp}(E) \propto (v/c) \exp[-0.2938(\gamma-1) - 0.0144(\gamma-1)^2] \quad (5.21)$$

at  $L=1.765$ . This is the spectrum of energies that results from the beta decay of nuclear-fission products in equilibrium. The pitch-angle-diffusion lifetimes  $\tau(L)$  are assumed to be given by linear interpolation between  $\tau(1.5)=470$  days and  $\tau(2.1)=20$  days (cf. Fig. 41, Section IV.3) for all values of  $M$ . When (5.08) is solved for the evolution of  $F(L,t)$  using each of several trial values of  $D_{LL}$ , it is found that the best agreement with observation corresponds to  $D_{LL} \approx 6 \times 10^{-6} \text{ day}^{-1}$  at  $L=1.76$  [70]. This value is identical with the magnitude  $\sim 6 \times 10^{-6} \text{ day}^{-1}$  obtained from the analysis assuming conservation of particle energy rather than  $M$  and  $J$  (see Section IV.6).

There exists an alternative to the arbitrary imposition of boundary conditions outside the interval of  $L$  covered by the data. It is possible instead to obtain a realistic set of time-dependent boundary conditions directly from the data. Imposed at  $L_1$  and  $L_2$  ( $=3.4$  and  $4.8$ , respectively, in Fig. 74, Section V.4), these boundary conditions are suitable for

testing the validity of a tentatively established set of transport coefficients  $D_{LL}$  and  $\tau(L)$  via temporal integration of (5.08).

The initial conditions for this temporal integration of (5.08) are given by the observational values of  $F(L, t_1)$ , where  $t_1$  corresponds to 22 December. Two apparently incompatible sets of transport coefficients have been identified above for electrons having  $M = 750$  MeV/gauss following the December 1962 magnetic storm. The variational method (Section V.5) yields  $D_{LL} = 6 \times 10^{-10} L^{10} \text{ day}^{-1}$  and  $\tau = \tau(L)$ , as given in Fig. 78, for the twenty-day interval beginning 22 December. The method of temporal integration with fixed boundary conditions outside the data interval (Section V.6) yields  $D_{LL} = 5 \times 10^{-9} L^{10} \text{ day}^{-1}$  for an assumed  $L$ -independent lifetime of 20 days over the ten-day interval beginning 20 December.

The results of temporal integration from  $t = t_1$  (22 December) for the evolution of  $F(L, t)$ , using the observed values of  $F(L_1, t)$  and  $F(L_2, t)$  as time-dependent boundary conditions, are shown in Fig. 80 [119]. The predictions based on the smaller  $D_{LL}$  (obtained by the variational method) are clearly in better agreement with the observational data ( $3.6 \leq L \leq 4.6$ ) than the predictions based on  $D_{LL} = 5 \times 10^{-9} L^{10} \text{ day}^{-1}$ , when the twenty-day interval is viewed as a whole. Only during the first few days of the integration interval (*i.e.*, prior to Day 360) is there a hint that the value  $D_{LL} = 6 \times 10^{-10} L^{10} \text{ day}^{-1}$  might be inadequate.

According to Fig. 79, the larger value of  $D_{LL} = 5 \times 10^{-9} L^{10} \text{ day}^{-1}$  should have applied only to the ten-day interval beginning 20 December, rather than the twenty-day interval beginning 22 December. However, the lifetime function  $\tau(L)$ , as given in Fig. 75 (Section V.4), is found to vary by at least a factor of seven between  $L = 3.6$  and  $L = 4.6$  for any reasonable choice of  $D_{LL}$ . Thus, it is appropriate to test  $D_{LL} = 5 \times 10^{-9} L^{10} \text{ day}^{-1}$  in conjunction with the lifetime function  $\tau(L)$ , as given in Fig. 75 or 78. For  $\tau(L)$  given by Fig. 78 and  $D_{10} = 5 \times 10^{-9} \text{ day}^{-1}$ , the temporal integration of (5.08) with time-dependent boundary conditions at  $L_1 = 3.4$  and  $L_2 = 4.8$  from  $t = 0$  (20 December) is found to produce good agreement with the observations ( $3.6 \leq L \leq 4.6$ ) until about 25 December (see Fig. 81). During this six-day interval, the smaller value of  $D_{10} = 6 \times 10^{-10} \text{ day}^{-1}$  is clearly inadequate to account for the continuing growth of  $F(L, t)$  at the lower  $L$  values ( $L \lesssim 4.2$ ). The discrepancy beyond 25 December can be eliminated by reverting to the smaller value of  $D_{10}$  (*cf.* Fig. 80).

These results clearly demonstrate that a time dependence of  $D_{LL}$  was associated with the large magnetic storm of 17–18 December 1962. The choice of 22 December as  $t_1$  apparently eliminates most of the storm-time effects that would invalidate the variational method

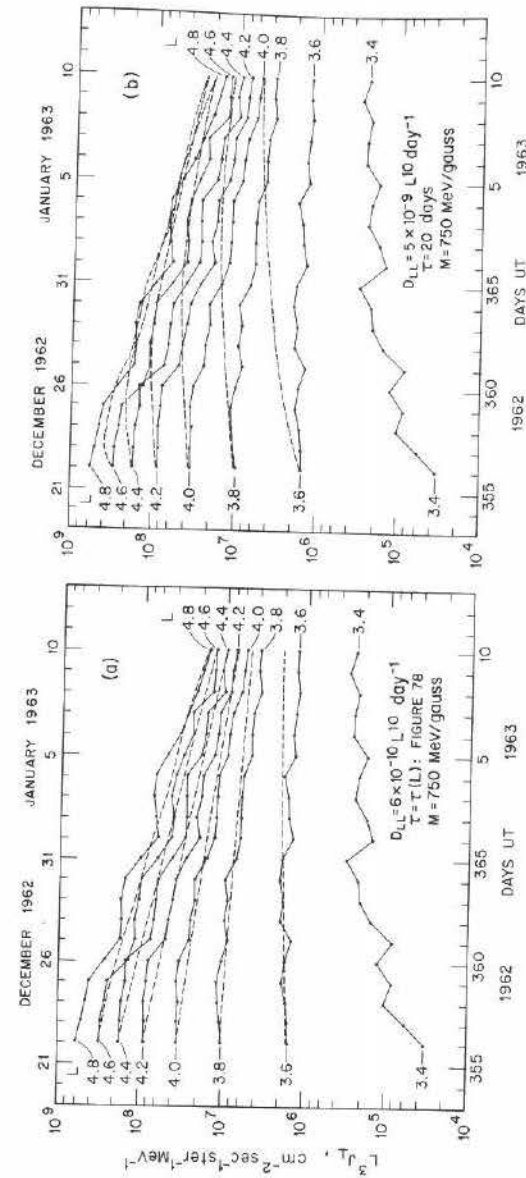


Fig. 80. Evolution of  $L^3 J_L$  for outer-zone electrons, beginning with 22 December 1962. Observational data points joined by solid line segments are taken from Fig. 74. Dashed curves are predictions generated by numerical integration with time-dependent boundary conditions imposed by the data at  $L = 3.4$  and  $L = 4.8$  [119].

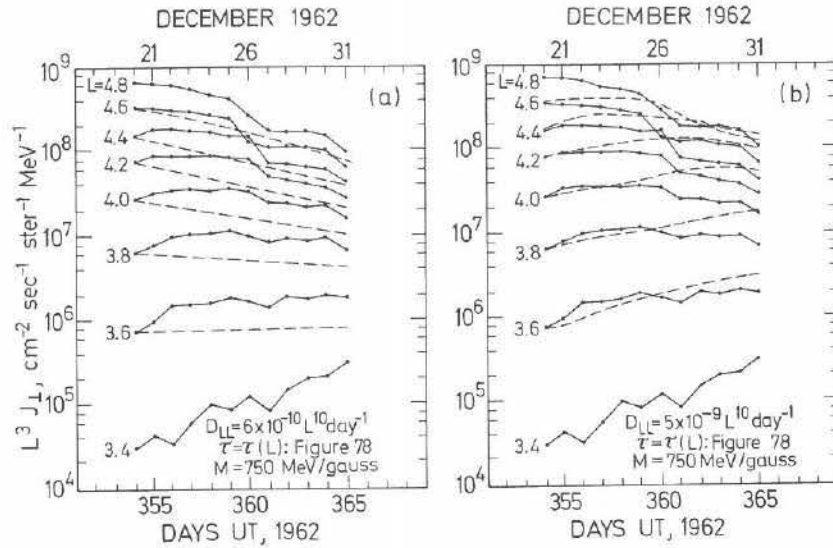


Fig. 81. Evolution of  $L^3 J_{\perp}$  for outer-zone electrons, beginning with 20 December 1962. Observational data points are joined by solid line segments. Dashed curves are predictions generated by numerical integration with time-dependent boundary conditions imposed by the data at  $L=3.4$  and  $L=4.8$  (cf. Fig. 80).

in its present form (Section V.5). Application of the variational method to the time interval 20–24 December would perhaps yield the larger diffusion coefficient  $D_{LL}$  evidently required for that interval, if by some means the data were smoothed to suppress adiabatic and other temporal fluctuations not associated with the radial and pitch-angle diffusion processes. It is evidently impossible, however, to characterize the radial diffusion coefficient as a universal constant that can be applied uncritically to time periods during and following all magnetic storms.

A set of proton measurements, made with a scintillation counter on the elliptical-orbit satellite Explorer 26, revealed time variations in the outer-zone proton fluxes following the magnetic storm of 18 April 1965. After removal of the adiabatic variations (due to the storm-time ring current, cf. Section I.5) from the observations, non-adiabatic changes in flux were found to have occurred during the storm. Thereafter the fluxes slowly recovered non-adiabatically to their pre-storm levels. These non-adiabatic post-storm observations can be attributed to radial diffusion and atmospheric collisions.

Examples of adiabatically-corrected  $L^3 \bar{J}_{\perp}/M$  profiles for equatorially-mirroring protons at several values of  $M$  were shown in Fig. 43 (Section IV.3). The data from several energy channels were used to

construct these constant- $M$  distribution functions, whose temporal evolution can be used to estimate a numerical value for the radial diffusion coefficient. In this case the diffusion equation has two separate loss terms. The first represents Coulomb energy loss [see (2.04) and (2.06), Section II.2; also (3.57), Section III.8]. The second loss term is equal to  $-\bar{f}/\tau_q$ , where  $\tau_q$  is the mean proton lifetime against charge exchange [see (2.09), Section II.2]. Pitch-angle scattering of these outer-zone protons by plasma waves is apparently negligible except at  $M=45$  MeV/gauss.

The Fokker-Planck equation governing outer-zone protons having  $M \gtrsim 100$  MeV/gauss and  $J=0$  is thus of the form

$$\frac{\partial \bar{f}}{\partial t} = L^2 \frac{\partial}{\partial L} \left[ \frac{D_{LL}}{L^2} \frac{\partial \bar{f}}{\partial L} \right]_M + \frac{(4\pi q^4/m_e)}{(2MB_0^3/L^9 m_p)^{1/2}} \left[ \frac{\partial(C\bar{f})}{\partial M} \right]_L - \frac{\bar{f}}{\tau_q}, \quad (5.22)$$

where  $C$  is given by (3.57b). Time-dependent boundary conditions for the solution of (5.22) are imposed by the observational data at  $L_1=2.1$  and  $L_2=5.6$ . Preliminary results suggest that an  $M$ -independent radial-diffusion coefficient  $D_{LL} \sim 1 \times 10^{-9} L^{10} \text{ day}^{-1}$  adequately accounts for the observed temporal evolution of  $\bar{f}(M, L; t)$  at  $J=0$  for  $L_1 < L < L_2$  [82].

## V.7 Spatial Integration

When the observational data consist of time-independent flux profiles  $\bar{J}_{\perp}(E, L)$ , it is necessary to obtain the relevant time-independent solution of the Fokker-Planck equation. If the transport coefficients and boundary conditions are time-independent, then the solution  $\bar{f}(M, J, L; t)$  for (5.22) and similar equations will ultimately approach the steady-state solution  $\bar{f}(M, J, L; \infty)$  after a sufficiently long integration time. In many situations, however, it is computationally more practical to dispense with temporal integration altogether by setting  $\partial \bar{f}/\partial t = 0$  at the outset. The result is a partial differential equation in the variables  $L$  and  $M$  (perhaps also  $J$ ). One problem often treated in this manner is that of the inner proton belt, as described by (3.57) [see Section III.8].

Substantial theoretical effort has been expended on identifying the possible sources of the high-energy ( $E \gtrsim 20$  MeV) proton radiation observed in the inner zone at  $L \lesssim 2$ . Much of this theoretical work has focused on attempts to vindicate the decay of cosmic-ray-produced albedo neutrons (CRAND) as the predominant source (see Section III.8). When radial diffusion is neglected, it is found that the CRAND-source hypothesis cannot successfully account for the observed absolute

intensities, nor the spatial and spectral distributions of inner-zone protons. However, a reasonable fit to the observed high-energy inner-zone proton distributions can be obtained when radial diffusion and the geomagnetic secular variation (see Section II.2) are allowed to operate on protons injected by the CRAND source.

The most extensive inner-zone proton data assembled to date were obtained by a set of shielded semiconductor detectors flown on the United States Air Force satellite OV3-4 as an investigation for biological purposes. These integral proton-flux data, measured above five energy thresholds (15 MeV, 30 MeV, 55 MeV, 105 MeV, and 170 MeV), can be converted to equivalent equatorial profiles of  $\bar{J}_\perp/MB \equiv 2m_0\bar{f}$  for selected values of the first invariant  $M$ . The results are plotted as the data points in Fig. 82.

If the geomagnetic secular variation is tentatively neglected, the time derivative  $\partial\bar{f}/\partial t$  appearing in (3.57) can be set equal to zero in the search for a steady-state distribution  $\bar{f}(M,L)$ . The source term  $S$  is considered to be given by (3.56), and the loss term represents proton

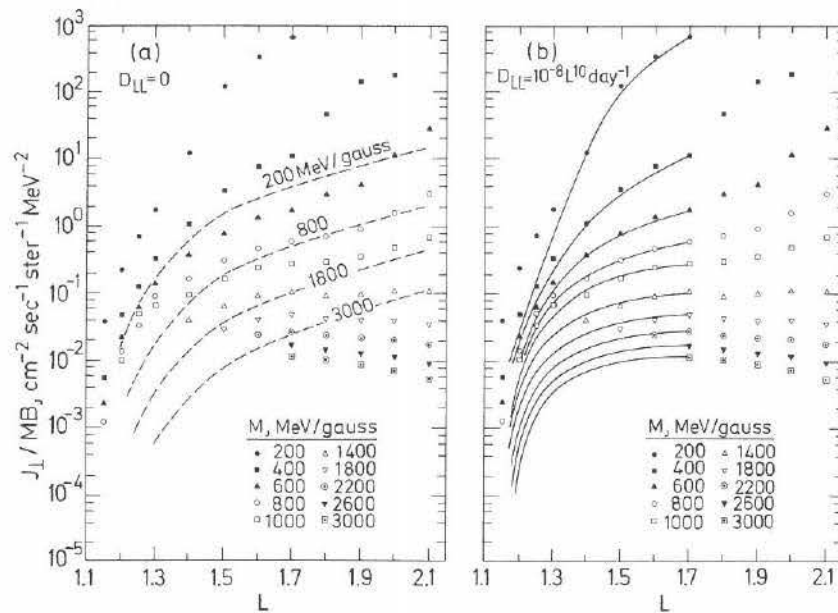


Fig. 82. Inner-zone proton distribution function ( $\times 2m_0$ ) for  $J=0$  and selected values of  $M$ , based on OV3-4 data and numerical integration. Dashed curves (a) are steady-state solutions of (3.57) for  $D_{LL}=0$  and  $S$  given by (3.56). Solid curves (b) are steady-state solutions of (3.57) for  $D_{LL}=10^{-8} L^{10} \text{ day}^{-1}$ , with  $S$  given by (3.56) and boundary conditions imposed by the data at  $L=1.1$  (where  $\bar{f}=0$ ) and  $L=1.7$  [38].

energy loss by collisions with free and bound atmospheric electrons (see Section II.2). Charge exchange is a negligible process at the proton energies of interest (cf. Fig. 15, Section II.2).

If radial diffusion is neglected (by taking  $D_{LL}=0$ ), then (3.57) becomes an ordinary first-order differential equation for  $\bar{f}(M)$  at each  $L$  value. A unique solution is obtained by requiring that  $C\bar{f}$  vanish in the limit  $M=\infty$ . This solution, indicated by the dashed curves in Fig. 82a, bears little resemblance to the observational data [38].

In the presence of a nonvanishing  $D_{LL}$ , it becomes necessary to specify boundary conditions in  $L$  as well as in  $M$ . Since the purpose is to verify the adequacy of the CRAND source, the lower boundary condition should be that  $f(M,L)$  vanish at some  $L=L_1 \approx 1.10$ . This lower boundary condition identifies the dense atmosphere as a sink for the inner-belt protons, and yet does not conflict with the observation that  $\bar{f}(M,L) \neq 0$  at  $L=1.15$ . The upper boundary condition is imposed by the observational data at  $L_2=1.70$ , beyond which temporal variations of  $\bar{f}(M,L)$  are known to occur. For computational convenience it is assumed that  $\bar{f}(M,L)=0$  at  $M=4 \text{ GeV/gauss}$  (rather than  $M=\infty$ ) throughout the interval  $L_1 \leq L \leq L_2$ . The solution thus obtained by choosing  $D_{LL}=1 \times 10^{-8} L^{10} \text{ day}^{-1}$  is indicated by the solid curves in Fig. 82b [38]. A vast improvement in the agreement between theory and observation is thus obtained by allowing the CRAND source to be complemented by protons diffusing inward from the outer zone.

A further improvement is expected to follow [39] from inclusion of the geomagnetic secular variation (see Section II.2). A correct treatment will require the use of (3.57) in its time-dependent form, with the Coulomb energy-loss rate expressed as a function of  $M$ ,  $\Phi$ , and  $t$ . It may be difficult to model the time dependence of  $D_{\phi\psi}$  and the boundary conditions on  $\bar{f}(M,L;t)$  over a history that extends at least back to Biblical times, but such an extrapolation seems necessary in order to account fully for protons now present in the inner belt. Even with the secular effect omitted (as in Fig. 82b), however, reasonable agreement between theory and observation has been obtained by allowing the generally accepted CRAND proton source [72] to operate in the presence of radial diffusion<sup>56</sup>.

<sup>56</sup>Recent measurements suggest that the actual neutron flux exceeds the previously accepted value [72] by a factor  $\sim 50$  at each energy above  $\sim 50 \text{ MeV}$  [87].